Renewable Energy 55 (2013) 305–321

Contents lists available at SciVerse ScienceDirect

Renewable Energy

journal homepage: www.elsevier.com/locate/renene

Wave energy resources along the Hawaiian Island chain

Justin E. Stopa [a], Jean-François Filipot [a,1], Ning Li [a], Kwok Fai Cheung [a,*], Yi-Leng Chen [b], Luis Vega [c]

[a] Department of Ocean and Resources Engineering, University of Hawaii at Manoa, Honolulu, HI 96822, USA
[b] Department of Meteorology, University of Hawaii at Manoa, Honolulu, HI 96822, USA
[c] National Marine Renewable Energy Center, University of Hawaii at Manoa, Honolulu, HI 96822, USA

ARTICLE INFO

Article history:
Received 24 January 2012
Accepted 12 December 2012
Available online

Keywords:
Hawaii
Spectral wave models
Mesoscale model
Wave atlas
Wave energy
Wave power

ABSTRACT

Hawaii's access to the ocean and remoteness from fuel supplies has sparked an interest in ocean waves as a potential resource to meet the increasing demand for sustainable energy. The wave resources include swells from distant storms and year-round seas generated by trade winds passing through the islands. This study produces 10 years of hindcast data from a system of mesoscale atmospheric and spectral wave models to quantify the wind and wave climate as well as nearshore wave energy resources in Hawaii. A global WAVEWATCH III (WW3) model forced by surface winds from the Final Global Tropospheric Analysis (FNL) reproduces the swell and seas from the far field and a nested Hawaii WW3 model with high-resolution winds from the Weather Research Forecast (WRF) model capture the local wave processes. The Simulating Waves Nearshore (SWAN) model nested inside Hawaii WW3 provides data in coastal waters, where wave energy converters are being considered for deployment. The computed wave heights show good agreement with data from satellites and buoys. Bi-monthly median and percentile plots show persistent trade winds throughout the year with strong seasonal variation of the wave climate. The nearshore data shows modulation of the wave energy along the coastline due to the undulating volcanic island bathymetry and demonstrates its importance in selecting suitable sites for wave energy converters.

1. Introduction

The Earth's changing climate, the increasing cost of oil, and the finite supply of fossil fuels have created social, economic, and political pressure for alternative sources of energy. Public and private industries across the globe are actively using, developing, and testing technologies to extract *clean* energy. Hawaii's high concentration of population and isolated location in the Pacific provides the perfect backdrop for development of renewable energy resources. The state legislature passed the Clean Energy Initiative in 2008 with the goal of reaching 70% clean energy by the year 2030. Energy technologies utilizing wind and solar resources are commercially available and used across the state. There is a reignited interest in ocean waves as a potential resource for the production of electricity in Hawaii. Research and development work on wave energy conversion (WEC) devices, which had begun much earlier around the world, has produced many designs and prototypes ready for sea trials [1,2]. The devices planned for Hawaii operate in approximately 50 m water depth outside the surf zone and yet are close to the shore for mooring and maintenance as well as connection to the power grid.

Throughout the world Hawaii is known for its powerful waves and its marine recreational activities. Hidden in these activities are the wave energy resources and the research opportunities to understand the ocean environment. The mid-Pacific location and massive archipelago provide an excellent tapestry to study the unique wave climate not seen in other places. Fig. 1 illustrates the climate pattern of the wind waves and swells around the major Hawaiian Islands. The multi-modal sea state in Hawaii provides an indicator of the weather from the far-reaching corners of the Pacific [3]. Extratropical storms near the Kuril and Aleutian Islands generate northwest swells reaching 5 m significant wave height in Hawaii waters during November through March. The south-facing shores experience more gentle swells generated by the year-round Westerlies in the Southern Hemisphere that are augmented by mid-latitude cyclones off Antarctica during May through September [4]. In addition, the consistent trade winds generate wind waves from the northeast to east throughout the year. The Hawaiian Islands modify the trade wind flow and create

* Corresponding author.
E-mail addresses: stopa@hawaii.edu (J.E. Stopa), jean-francois.filipot@shom.fr (J.-F. Filipot), ningli@hawaii.edu (N. Li), cheung@hawaii.edu (K.F. Cheung), yileng@hawaii.edu (Y.-L. Chen), luisvega@hawaii.edu (L. Vega).
[1] Present address: Service Hydrographique et Océanographique de la Marine, Brest CEDEX 2, France.

0960-1481/$ – see front matter © 2013 Elsevier Ltd. All rights reserved.
http://dx.doi.org/10.1016/j.renene.2012.12.030

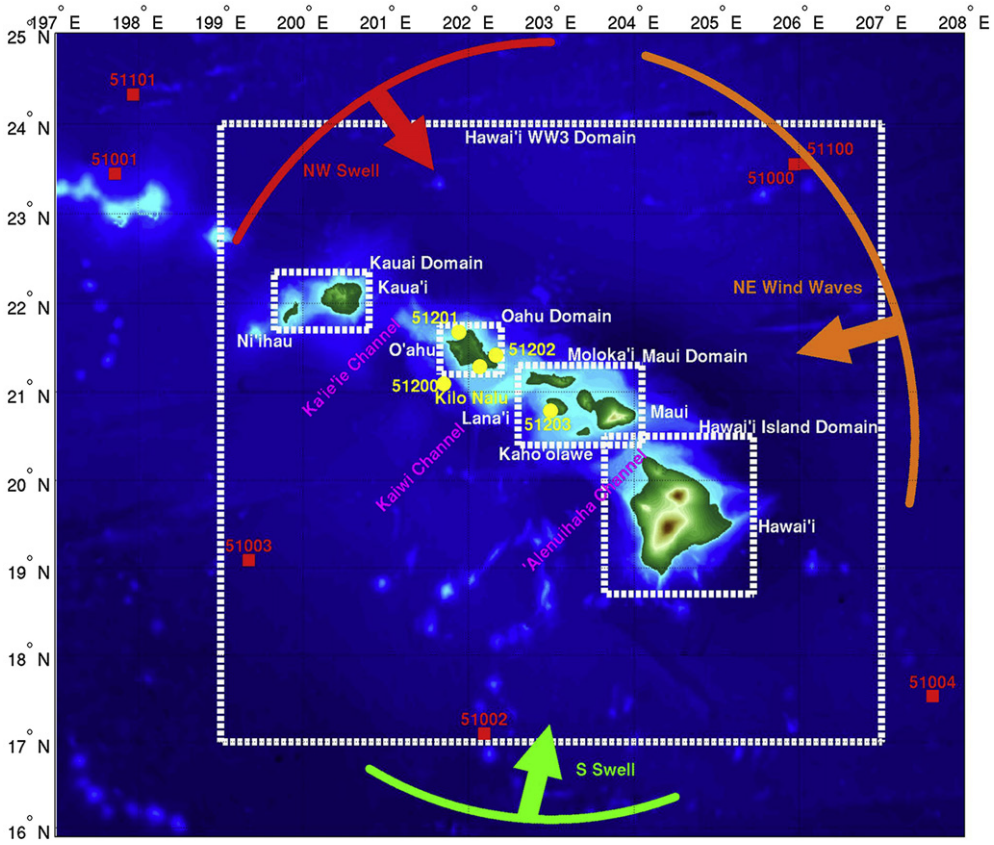

Fig. 1. Wave climate, buoy resources, and nested computational domains around the Hawaiian Islands.

localized weather patterns [5]. Knowledge of the regional wave climate and the coastal wave resources is a prerequisite in the selection of suitable sites for testing and operations of wave energy converters. However, the available buoys as shown in Fig. 1 provide wave data either far offshore of the island chain or at nearshore locations not directly relevant for most potential sites.

Third generation spectral wave models, which can describe multi-modal sea states, have emerged as a reliable tool for forecasting and hindcasting ocean conditions. These models account for random sea states under the action of winds by evolving the energy density spectrum in time and space for a range of wave frequencies and directions. The National Centers for Environmental Prediction (NCEP) operates the third generation spectral wave model WAVEWATCH III (WW3) to provide 7.5 days of global wave forecasts at 0.5° resolution [6,7]. This operational model is forced with assimilated surface winds from the Global Forecast System (GFS) [8]. The European Centre for Medium Range Weather Forecasts (ECMWF) operates the integrated Forecast System (IFS), which consists of an atmospheric model coupled with the spectral wave model WAM [9] to produce 10-day forecasts at 0.36° resolution. The use of these operational models in hindcast mode allows assessment of the global wave climate and energy resources. Caires et al. [10] compiled IFS reanalysis data over the period 1971–2000 to provide a 1.5° × 1.5° atlas of global winds and waves. Arinaga and Cheung [3] produced a 1.25° × 1° global atlas of wind wave and swell energy using WW3 and NCEP's Final Global Tropospheric Analysis (FNL) winds from 2000 to 2009.

The resolution in the global wave models prevents proper descriptions of the wave conditions near the shore and can lead to significant errors along an archipelago as demonstrated by Ponce de Leon and Guedes Soares [11] and Rusu et al. [12]. Recent studies have used spectral wave models at higher resolution with interpolated global wind data to provide assessment of regional or coastal wave resources in Europe [13–15], North America [16,17], and Australia [18]. The Hawaii archipelago, however, modifies the trade wind flow and creates localized weather patterns that must be considered in spectral wave modeling. Stopa et al. [19] utilized a two-way nested global and Hawaii WW3 model to examine the effects of local winds on wave energy resources in two case studies representative of winter and summer conditions. The FNL data provides the global wind forcing as well as the initial and boundary conditions to produce high-resolution regional winds from the Weather Research and Forecast (WRF) model [20]. The Hawaii WRF model describes mesoscale phenomena such as diurnal thermal forcing of sea and land breezes [21], flow acceleration and deceleration around topographic features, and wake formation on the leeside of islands [5]. The speed-up of the winds in channels and around headlands augments the far-field wave energy and creates wave conditions that are known to be treacherous to mariners.

The present study continues the effort of Stopa et al. [19] and Arinaga and Cheung [3] by utilizing the Simulating WAves Nearshore (SWAN) model of Booij et al. [22] at each major island in

Table 1
Setup of nested computational domains for spectral wave modeling.

	Lower Lon. (°E)	Upper Lon. (°E)	Lower Lat. (°N)	Upper Lat. (°N)	Resolution (°)	Resolution (km)
Global WW3	0.00	360.00	−90.00	90.00	1.25 × 1.00	138 × 111
Hawaii WW3	199.00	207.00	17.00	24.00	0.05 × 0.05	5.6 × 5.6
Kauai SWAN	199.65	200.80	21.70	22.35	0.005 × 0.005	0.56 × 0.56
Oahu SWAN	201.65	202.40	21.20	21.75	0.005 × 0.005	0.56 × 0.56
Maui SWAN	202.60	204.10	20.40	21.30	0.01 × 0.01	1.1 × 1.1
Hawaii SWAN	203.80	205.30	18.85	20.35	0.01 × 0.01	1.1 × 1.1

Hawaii and extending the hindcast study to provide a continuous dataset from 2000 to 2009. The high-resolution Hawaii WW3 accounts for local winds and island shadowing to provide an accurate description of the complex wave pattern along the island chain. The SWAN model is better suited for nearshore environments due to the implicit numeric scheme and the ability to account for triad wave interactions in shallow water. It can account for some effects of diffraction by including an additional term derived from the mild-slope equation [23]. Filipot and Cheung [24] recently provided additional parameterizations of energy dissipation due to wave breaking and bottom friction for the fringing reef conditions of Hawaii. Wind and wave data derived from satellite and buoy measurements allows validation of the hindcast WRF and WW3 data around Hawaii. The 10 years of validated hindcast data provides a wealth of information to elucidate the wind and wave climate and develop high-resolution wind and wave atlas in Hawaii. The nearshore data from SWAN describes the wave energy resources in the form of bi-monthly median and percentile plots to provide precise information for planning and design of wave energy converters along the island coasts.

2. Methodology

2.1. Model setup

The present study utilizes a system of nested global, regional, and island-scale spectral wave models based on WW3 of Tolman et al. [6,7] and SWAN of Booij et al. [22] with wind forcing from the NOAA Final Global Troposphere Analysis (FNL) and a WRF model resolving the major Hawaiian Islands. Fig. 1 illustrates the setup of the nested wave models. Four island-scale SWAN domains are nested within the Hawaii WW3 domain, which in turn is nested inside a global WW3 domain. Table 1 lists the coverage and resolution of each computational grid. The series of nested grids capture physical processes at increasing temporal and spatial resolution toward Hawaii. The system is automated through a set of scripts, which link the model components with databases and utility programs to provide high-resolution wind and wave data. The same system is also in operation to provide 7.5-day high-resolution forecasts of wind and wave conditions around Hawaii (http://oceanforecast.org/).

The key to the entire modeling process is accurately describing the input wind field. The Global Forecast System (GFS) is a spectral model with 0.5° spatial resolution on the earth surface and 64 layers extending to the top of the atmosphere [8]. NCEP runs the model four times daily with assimilation of observational data from land stations and satellites to forecast the atmospheric conditions on a real-time basis [25]. The FNL data, which is derived from GFS on a $1^\circ \times 1^\circ$ grid at 0000, 0600, 1200, and 1800, provides the initial and boundary conditions to Hawaii WRF [26]. The WRF model is based on the non-hydrostatic, three-dimensional Euler equation in the sigma vertical coordinate. In the regional implementation, the Noah LSM (NCEP, Oregon State University, Air Force, and Hydrological Research Laboratory Land Surface Model) accounts for vegetation coverage and land surface properties using data compiled by Zhang et al. [26]. The computational domain extends from 194–210°E and 16–26°N beyond Hawaii WW3 to model the upstream flow from the trade winds and the modified wind field downstream of the islands. The 6 km grid spacing is sufficient to resolve the physical processes important to local wind wave generation. The production consists of a series of overlapping 36-h runs with the data output at the standard 10 m elevation every hour. The first 12 h allows spin-up of the regional model from the boundary condition and the remaining 24 h is archived to produce a continuous 10-year dataset of the wind velocity.

WW3 is a third generation spectral wave model developed by Tolman et al. [6,7]. The phase-averaged model evolves the action density N for a range of frequencies f and 360° of directions θ under wind forcing and geographical constraints. It is governed by the action balance equation and when written in the latitude and longitude (ξ, ψ) spherical coordinates, is given by

$$\frac{\partial N}{\partial t} + \frac{1}{\cos\xi}\frac{\partial}{\partial \xi}\dot{\xi} N\cos\theta + \frac{\partial}{\partial \psi}\dot{\psi} N + \frac{\partial}{\partial k}\dot{k} N + \frac{\partial}{\partial \theta}\dot{\theta} N = \frac{S}{\sigma} \tag{1}$$

where t denotes time, k is wave number, $\sigma = 2\pi f$ is intrinsic angular frequency, the over-dot represents the rate of change, and S denotes the source terms accounting for nonlinear effects such as wind–wave interactions, quadruplet wave–wave interactions, dissipation through whitecapping, and dissipation due to bottom friction. The WAM4 source terms [27], which are available in the latest release of WW3 (V3.14), are applied to account for these nonlinear processes. The directional wave energy spectrum is obtained from $F(f, \theta) = N(k,\theta)/\sigma$ through a Jacobian transform from k to f. The significant wave height and average period are defined as

$$H_s = 4\sqrt{\int_0^\infty \int_0^{2\pi} F(f,\theta)\mathrm{d}\theta\mathrm{d}f} \tag{2}$$

$$T_{02} = \sqrt{\frac{m_0}{m_2}} \tag{3}$$

where m_0 and m_2 are the zeroth and second moment of the wave energy spectrum. We implement Global WW3 at $1^\circ \times 1.25^\circ$ resolution and incorporate a nested Hawaii grid at 3′ (~5.5 km) resolution. An obstructions file accounts for energy lost at small islands that cannot be resolved in the global computational grid [28]. FNL provides a continuous dataset of wind velocity and ice coverage at six hours intervals for input into Global WW3. Spectral wave conditions are exchanged internally at the boundary of Hawaii WW3, which is forced by hourly Hawaii WRF winds to capture the local wave conditions.

The Hawaii WW3 defines the spectral boundary conditions for SWAN to model coastal wave transformation in four island-scale domains as shown in Fig. 1. The resolution of the computational grids ranges from 18″ (0.55 km) for Kauai and Oahu to 36″ (1.1 km) for Maui and Hawaii Island. High-quality bathymetry around the islands is available from LiDAR surveys at 3–4 m resolution down to 40 m depth and from multibeam surveys at 50 m resolution in deeper waters. SWAN is similar to WW3 in that it solves the action balance Eq. (1) with parameterization of nonlinear processes, but its implicit scheme provides a steady state solution at each time step. The model includes additional source terms for triad wave–wave interactions, depth-induced wave breaking, wave diffraction, and dissipation in beach and reef environments. The SWAN domains provide the wave power in coastal waters using

$$P = \rho g \int_0^\infty \int_{-\pi}^{\pi} C_g(f) F(f,\theta)\mathrm{d}\theta\mathrm{d}f \tag{4}$$

where ρ is the density of water, g is the acceleration due to gravity, C_g is group velocity. The wave climate in Hawaii always contains a mix of swells and wind waves; thus, this method provides a better representation of the wave power in comparison to the common approach of using a single wave height and period estimated from the wave spectrum.

2.2. Observational data for validation

The FNL wind data, which already includes available measurements, underwent extensive evaluations prior to its releases [8]. Arinaga and Cheung [3] implemented the data in Global WW3 and validated the computed wave parameters with satellite and buoy measurements around the globe. The high-resolution, regional wind and wave data produced in this study needs independent validation with actual measurements before its implementation in the resource assessment. Fig. 1 shows the locations of seven offshore and five nearshore buoys operated by the National Data Buoy Center (NDBC) and the University of Hawaii (UH). These buoys provide direct and continuous measurements of the wave conditions for comparison with the model output at discrete locations around Hawaii. Spatial data available for model validation includes wind measurements from QuikSCAT and altimetry wave measurements from Jason-1. These platforms provide valid measurements across a large spatial region under most atmospheric conditions.

QuikSCAT provides wind measurements over 90% of the ice-free ocean surface daily with errors of less than 2 m/s in speed and 20° in direction [29]. The polar orbiting satellite flies over Hawaii twice daily in ascending and descending passes. The 1800-km swath, which covers most of the island chain, has a nominal spatial resolution of 12.5 km to capture mesoscale features. The scatterometer on QuikSCAT pulses cloud-penetrating microwaves in the Ku band toward the earth and records the backscatter signal under a majority of weather conditions. The wind speed and direction at 10-m elevation can be estimated from an empirical relationship known as the Geophysical Model Function without taking into account second-order geophysical effects such as wave height and sea surface temperature. A land mask of at least 25 km removes erroneous values caused by coastal land and a multidimensional rain-flagging technique indicates the presence of rain, which may alter the microwave pulse and subsequently the recorded data. The Direction Interval Retrieval with Threshold Nudging technique gives a unique solution for the wind direction [30]. Gridded wind speeds of approximately 12.5 km provide a comparison with interpolated data from Hawaii WRF.

NASA's Jet Propulsion Laboratory (JPL) operates the Jason-1 satellite, which has been providing continuous global ocean conditions since December 2001. The polar orbiting satellite covers the earth surface from 66°S to 66°N in 254 passes every 10 days. A dual-frequency (C & Ku microwave bands) altimeter measures the sea surface elevation with errors of up to 3.9 cm. Other on board sensors correct for vapor and electron contents in the atmosphere and the ionosphere. Erroneous data near the coastlines due to contaminated signals by the presence of land are removed when appropriate. The significant wave height is an intrinsic property of the sea surface measurement and is estimated from the leading edge of the returned signal with errors of ±0.4 m or 10% of the significant wave height, whichever is larger [31]. A number of data products are available through the JPL Physical Oceanography Distributed Active Archive Center. This study utilizes the Geophysical Data Record, which is considered the most accurate because it is a fully validated product with precise orbits, rain flags, and corrections for instrument effects. Along-track, gridded Hs values with resolution of approximately 3 arcmin (~5.5 km) allow direct comparison with results from Hawaii WW3.

We use a number of error metrics to measure the difference between the observed and computed data within the Hawaii WRF and WW3 domains. These include the mean error or bias (ME), normalized root mean square error (NRMSE), correlation (COR), and scattered index (SI) given as

$$\mathrm{ME} = \frac{1}{N}\sum_{i=1}^{N}(X_{Pi} - X_{Oi}) \tag{5}$$

$$\mathrm{NRMSE} = \frac{\sum_{i=1}^{N}(X_{Pi} - X_{Oi})^2}{N(\max(X_O) - \min(X_O))} \tag{6}$$

$$\mathrm{COR} = \frac{\sum_{i=1}^{N}\left(X_{Pi} - \overline{X_P}\right)\left(X_{Oi} - \overline{X_O}\right)}{\sqrt{\sum_{i=1}^{N}\left(X_{Pi} - \overline{X_P}\right)^2}\sqrt{\sum_{i=1}^{N}\left(X_{Oi} - \overline{X_O}\right)^2}} \tag{7}$$

$$\mathrm{SI} = \frac{1}{\overline{X_O}}\sqrt{\frac{1}{N}\sum_{i=1}^{N}\left[(X_{Pi} - X_{Oi}) - \overline{(X_P - X_O)}\right]^2} \tag{8}$$

where the over bar denotes the mean, the subscripts O and P denote observed and computed data, and N denotes the number of data pairs. It should be reiterated that the observed data also contains errors and is simply used as a reference for comparison.

3. Winds in Hawaii

The main Hawaiian Islands, which extend from 19°N to 23°N, lie within the trade wind belt and experience winds throughout the year from the east to northeast [4]. The speed-up of the winds in the channels and around headlands modifies the wave energy near the coast. Before the climate patterns are discussed, the Hawaii WRF data is examined against available wind measurements. QuikSCAT, which flew over Hawaii 7914 times (with sufficient data) during the 10-year period, provides a comprehensive dataset for validation.

The WRF winds are interpolated in time and space to match those of QuikSCAT for computation of the error metrics. Fig. 2 displays the results for the 10 years of wind data. Hawaii WRF provides a good description of the wind field upstream of Hawaii, in the channels, and around headlands that is critical for local wave generation. In these areas, the mean error and the NRMSE are typically less than 0.5 m/s and 5%. The computed and observed data shows good correlation of 0.8 and little variability as indicated by a scatter index of 15%. The most significant discrepancy occurs in the wake region of Hawaii Island, where the simulated wind speed is up to 3.5 m/s or 22% lower than the QuikSCAT winds at the separation points. The low correlation and large variability imply the errors in the location and timing, instead of the strength, of the circulation. A deterministic model might not capture the stochastic processes in the wake. On the other hand, it is well known that QuikSCAT overestimates wind speed under weak and variable conditions and produce less reliable measurements in coastal waters. The nominal 12.5-km resolution of QuikSCAT is inadequate in describing the complex flow pattern in the wake [32–34], but nevertheless, such flow pattern is not conducive to wave generation.

Fig. 3 plots the bi-monthly median wind speed to illustrate the local weather pattern and its seasonal variation. The trade winds persist throughout the year with the strongest and most consistent period in the summer months, peaked at July and August. The presence of the islands cause deceleration of the trade wind flow on the windward shores, while the channel-parallel pressure gradients accelerate the flow downstream, especially in the 'Alenuihaha channel between Maui and Hawaii Island [19]. For mountains with peaks well above the trade wind inversion, such as Mauna Kea and Mauna Loa of Hawaii Island, orographic blocking generates distinct wakes on the leeside with a westerly return flow between a pair of

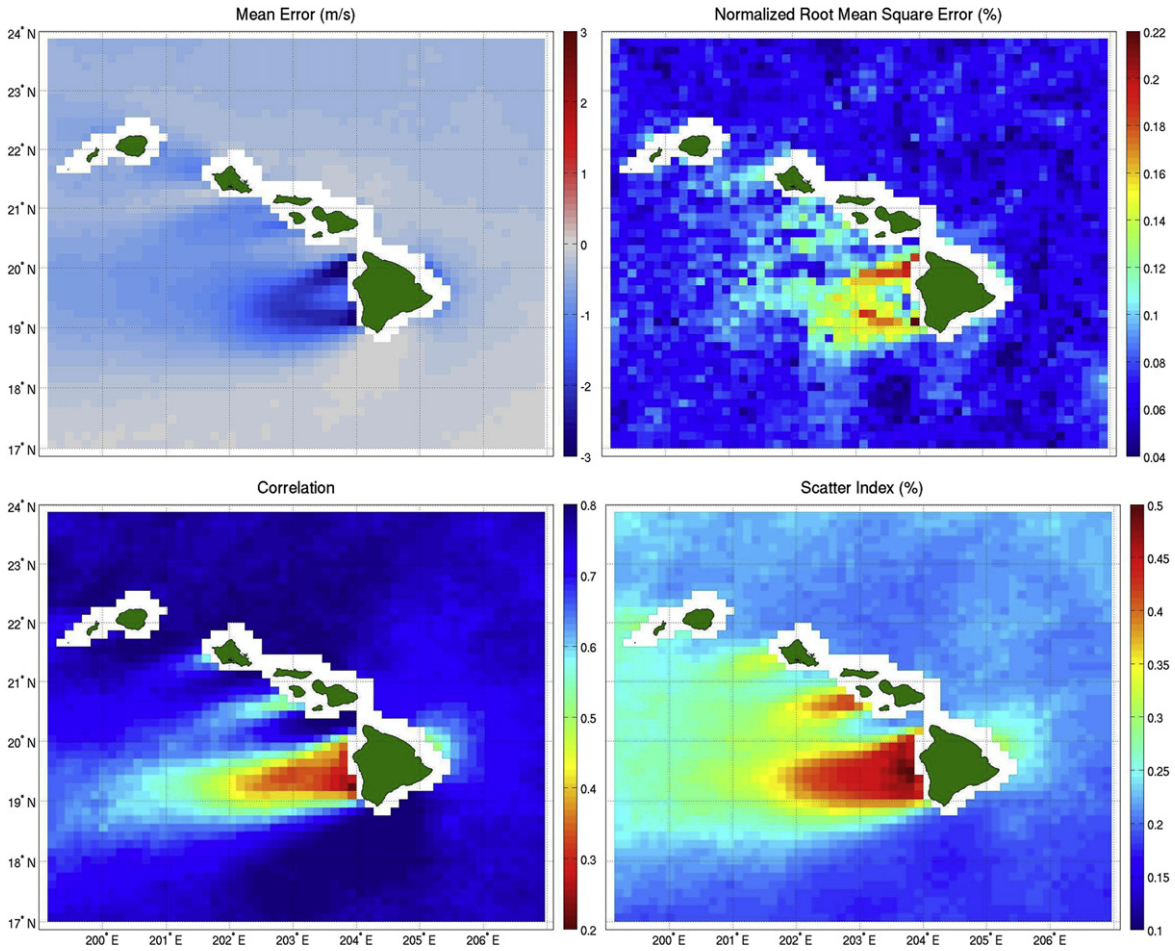

Fig. 2. Error metrics of wind speeds from Hawaii WRF and QuikSCAT.

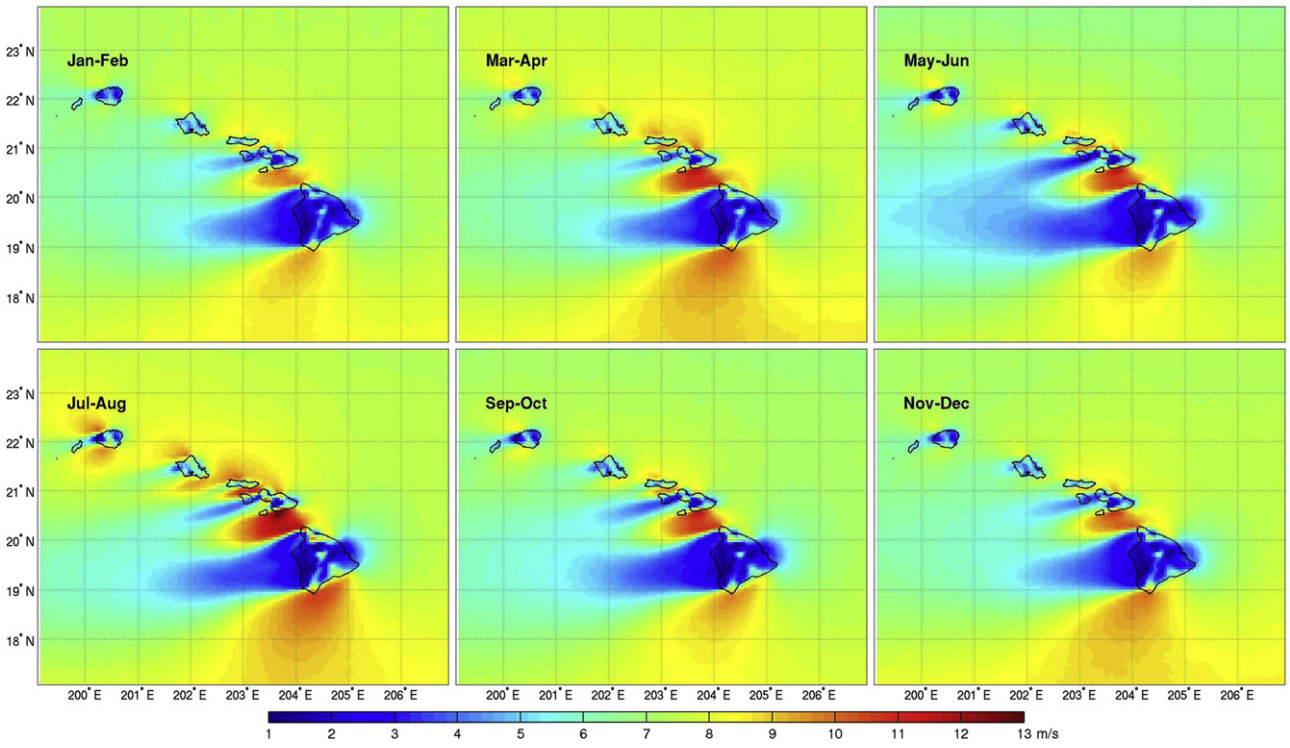

Fig. 3. Bi-monthly median wind speed from Hawaii WRF.

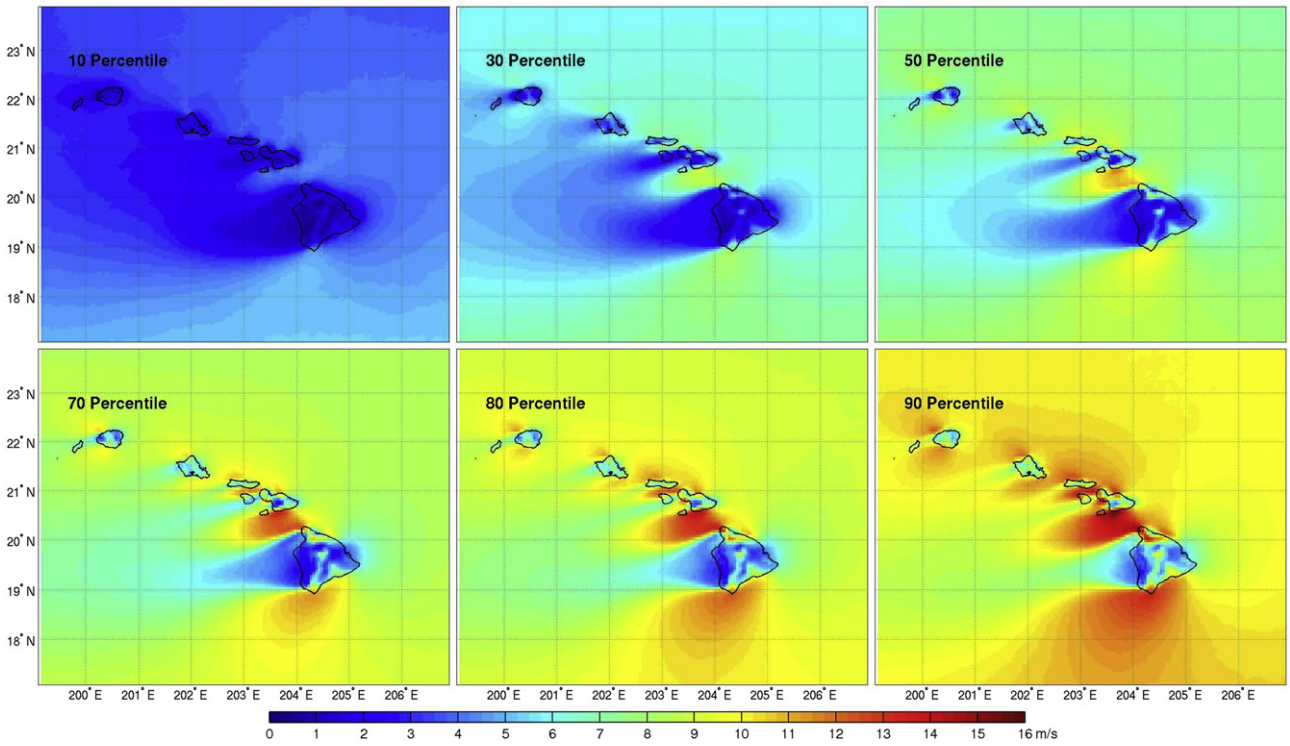

Fig. 4. Percentiles of wind speed from Hawaii WRF.

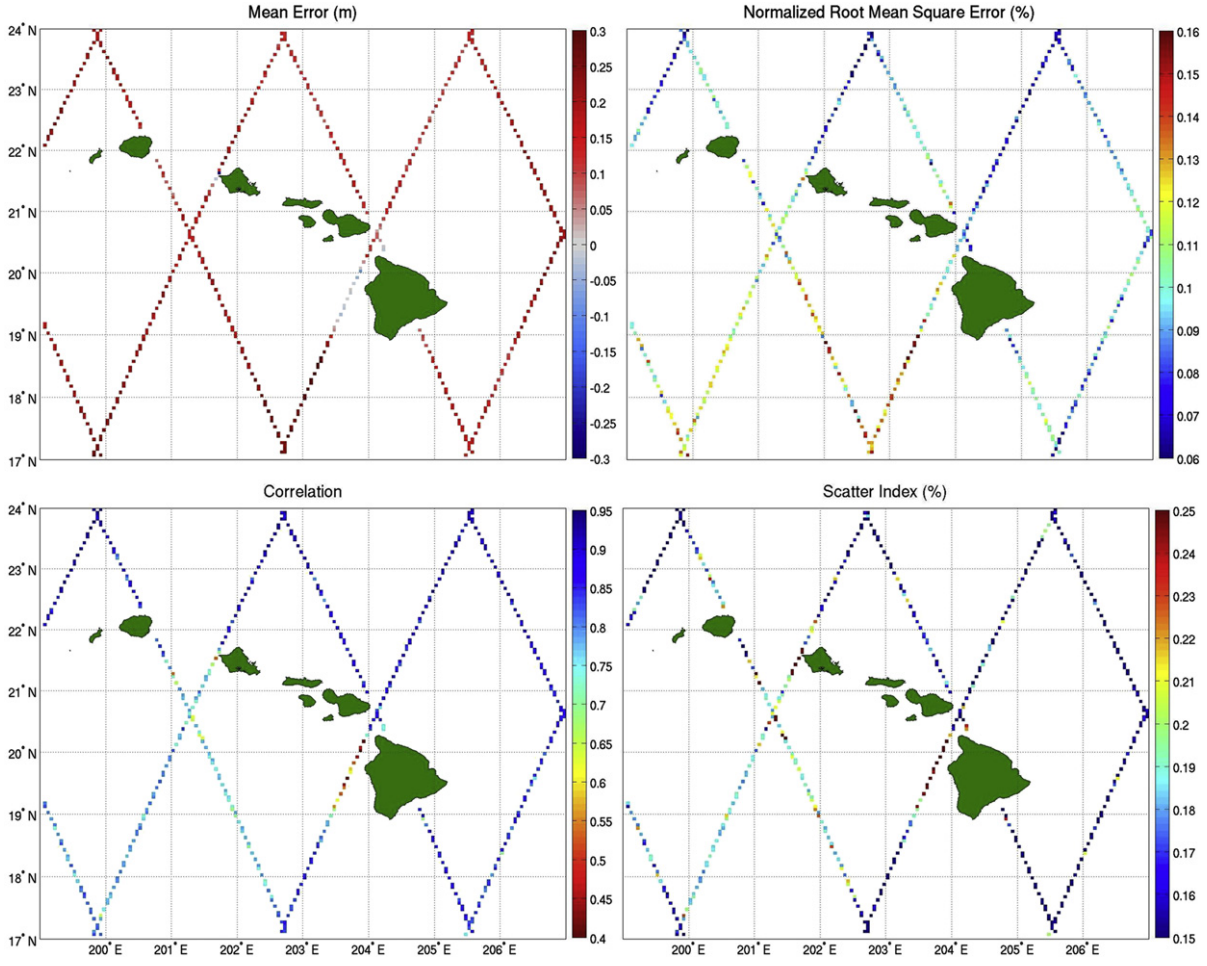

Fig. 5. Error metrics of significant wave heights from Hawaii WW3 and Jason-1.

counter-rotating lee vortices [32,33]. For smaller islands with mountain peaks well below the trade wind inversion, such as Kauai and Oahu, the wake zone is characterized by relatively weak winds; westerly flow only occurs in the coastal region during the daytime in response to land surface heating [33]. The winter months from November through February are susceptible to more variable trade winds due to the southward shift of the sub-tropical high pressure system toward Hawaii and occurrences of winter "Kona" storms [26,35]. These storms are infrequent and are not reflected in the median plots; however weakened wind speeds in these months are evident.

Wind speed statistics provide additional insights into the local climate and its effects on the wave resources. Fig. 4 presents the 10, 30, 50, 70, 80, and 90 percentiles of the computed wind speed. The results depict predominant trade wind flows from east to northeast with gradual strengthening in each successive percentile plot. The 50-percentile plot is very similar to the median May–June conditions with typical speeds of 8–12 m/s. All of the plots indicate up to 50% increase of the wind speeds on the north and south sides of the islands in relation to the upstream flow. The 90-percentile shows 14 m/s wind speeds in the channels and stronger winds extending leeward of Hawaii Island. The sufficiently high wind speed and long fetch can have an impact on the local wave energy during most of the year. The calm wake region extends across the entire domain. Effects from this wake have a lasting impact on the air–sea interaction 3000 km beyond the Hawaii archipelago [36].

4. Waves in Hawaii

The 10 years of hindcast data provides a wealth of information for wave climate research and resources assessment. Since Arinaga and Cheung [3] have already validated and examined the global wave data, we focus on the high-resolution data around Hawaii. The hindcast wave data is first validated with satellite and buoy measurements. We then present bi-monthly median and percentile plots of the significant wave height and average period to illustrate the wave climate in Hawaii.

4.1. Validation

The Jason-1 satellite flew across the Hawaii WW3 domain 2243 times (with sufficient data) during the 10-year period. The computed significant wave height is interpolated in time and space to compare with the altimetry measurements. Records from grid cells close to land may contain errors, but are included to assess the model performance in the under-sampled regions at the channels and near headlands. Fig. 5 plots the error metrics computed along the satellite tracks. The results show good agreement of the computed and measured data north of the island chain, which are

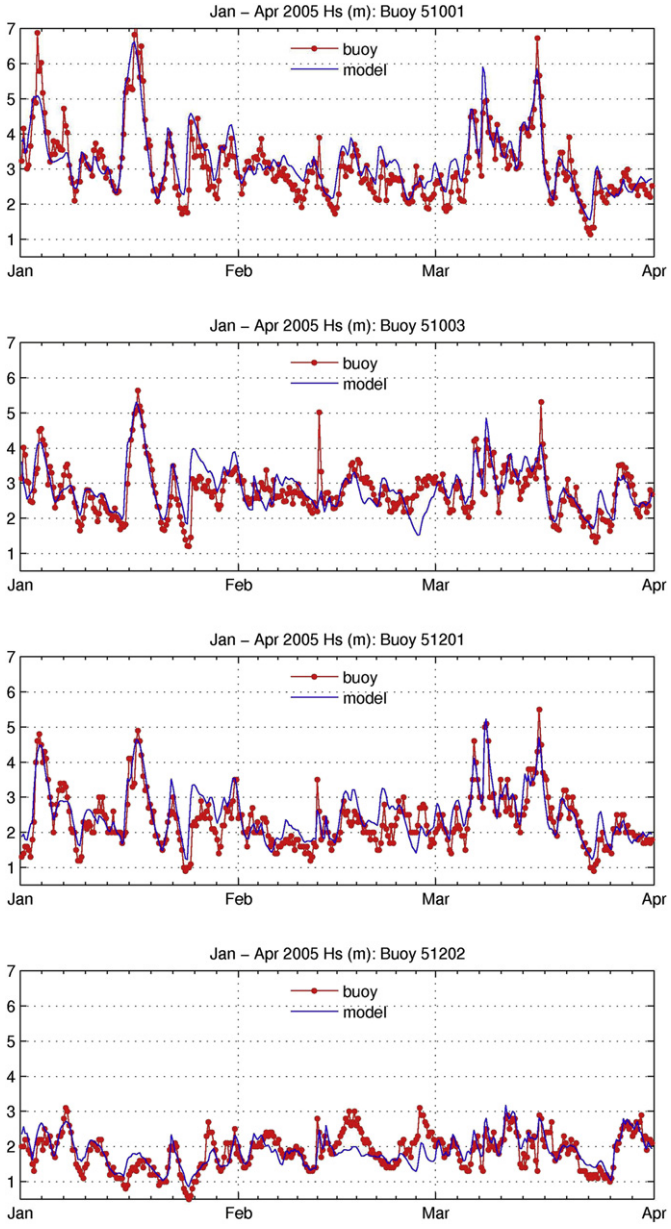

Fig. 6. Comparison of computed and recorded significant wave heights at representative buoys.

Table 2
Buoy information and error metrics.

Buoy	Domain	Start time	End time	Depth (m)	±Error (m)	ME (m)	RMSE (m)	NRMSE (%)	COR	SI (%)	Lin. fit slope
51001	Global WW3	Jan-02, 2000	Dec-24, 2009	3430	0.56	0.08	0.38	0.05	0.90	0.16	0.83
51002	Hawaii WW3	Jan-02, 2000	Dec-31, 2009	5002	0.59	0.11	0.39	0.07	0.80	0.15	0.81
51003	Hawaii WW3	Jan-02, 2000	Dec-31, 2009	4920	0.58	0.1	0.38	0.07	0.81	0.17	0.82
51004	Global WW3	Jan-02, 2000	Oct-07, 2009	5082	0.41	0.02	0.29	0.06	0.87	0.12	0.75
51100	Hawaii WW3	Apr-24, 2009	Dec-31, 2009	4755	0.56	0.26	0.44	0.08	0.89	0.16	0.88
51101	Global WW3	Feb-21, 2008	Dec-31, 2009	4792	0.63	0.26	0.49	0.07	0.88	0.19	0.82
51000	Hawaii WW3	Apr-24, 2009	Dec-31, 2009	4097	0.64	0.24	0.47	0.09	0.89	0.17	0.89
51200	Hawaii WW3	Oct-10, 2009	Dec-31, 2009	3150	0.60	0.28	0.47	0.11	0.84	0.18	0.86
51201	Oahu SWAN	Sep-08, 2004	Dec-31, 2009	198	0.54	0.09	0.35	0.06	0.90	0.2	0.92
51202	Oahu SWAN	Sep-08, 2004	Dec-30, 2009	100	0.43	0.09	0.29	0.06	0.89	0.14	0.86
51203	Maui SWAN	Jul-01, 2007	Dec-31, 2009	201	0.36	0.11	0.26	0.07	0.67	0.27	0.70
KNOH1	Oahu SWAN	Sep-01, 2008	Dec-31, 2009	12	0.30	0.09	0.23	0.09	0.59	0.28	0.60

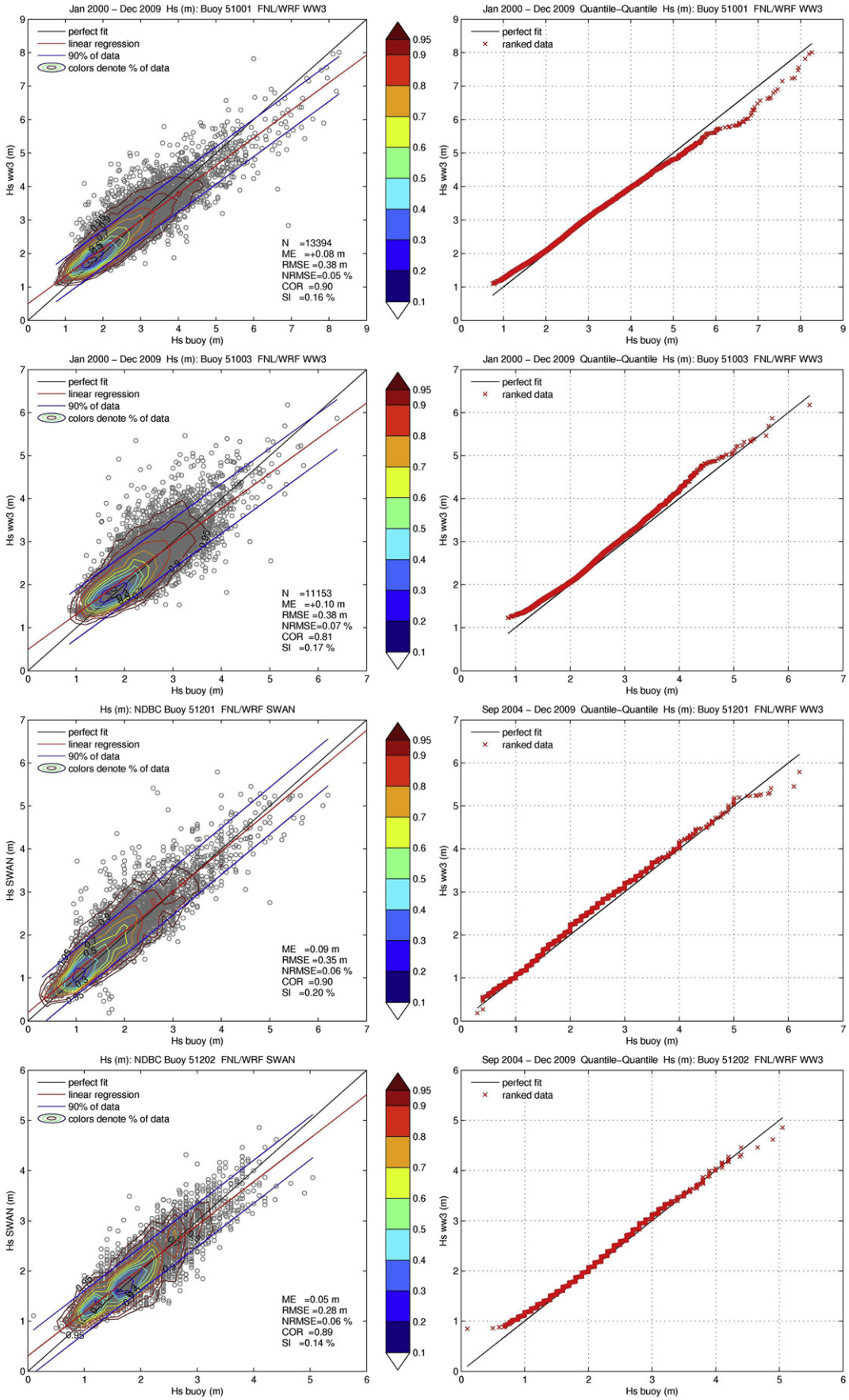

Fig. 7. Wave height validation with buoy measurements.

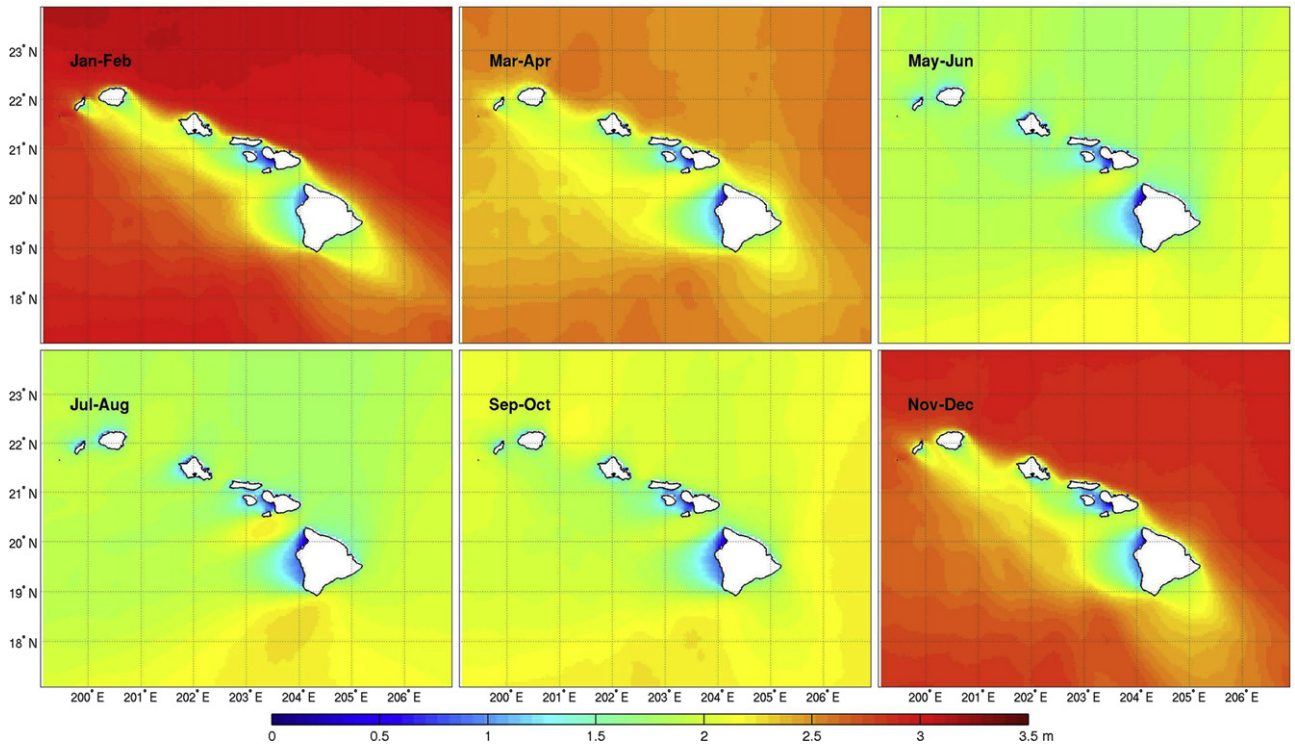

Fig. 8. Bi-monthly median significant wave height from Hawaii WW3.

directly exposed to the north swell and wind waves. The mean and normalized root mean square errors are within ±0.3 m and less than 10%. The correlation is above 0.9 and the scattered index is within 15%. Larger discrepancies, however, exist in the southern portion of the domain and in the channels. Correlation of 0.7, which is typical southeast of Kauai and southwest of Oahu and Maui, might be due to the lack of diffraction in WW3 to describe the energy in the shadows of the northwest swells and northeast wind waves. The track along the 'Alenuihaha Channel shows the lowest correlation with a negative bias. The errors are attributed to the

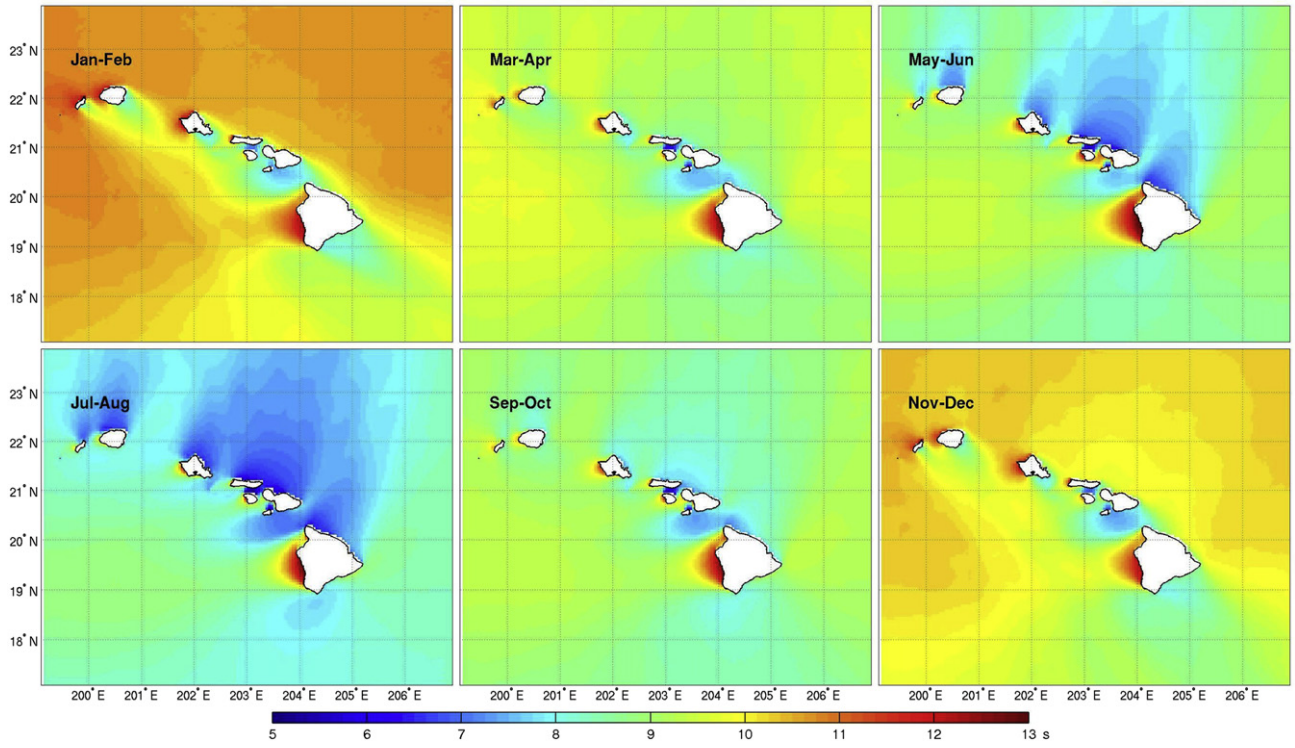

Fig. 9. Bi-monthly median average wave period from Hawaii WW3.

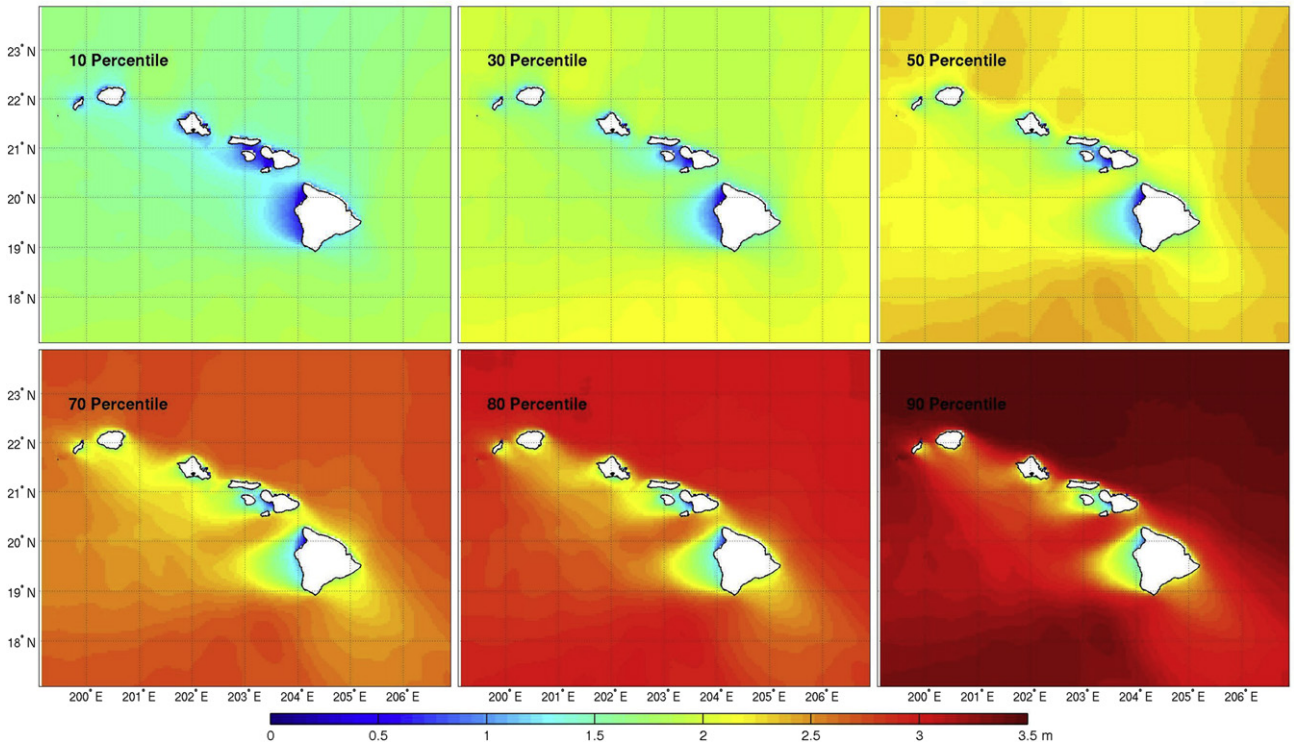

Fig. 10. Percentiles of significant wave heights from Hawaii WW3.

poorly resolved location and timing of the circulation in the trade wind wake leeward of Hawaii Island. This results in shifting of the wave field and energy level in time and space.

Measurements from 12 buoys around Hawaii are available to validate the hindcast data. Table 2 lists the buoy locations, water depths, and data periods ranging from 1 to 10 years. Fig. 6 plots a sample of the recorded and computed significant wave heights at four representative buoys for January–April 2005, during which Hawaii experienced several north swell and wind wave events. Buoy 51001 is fully exposed to the northwest swells approaching

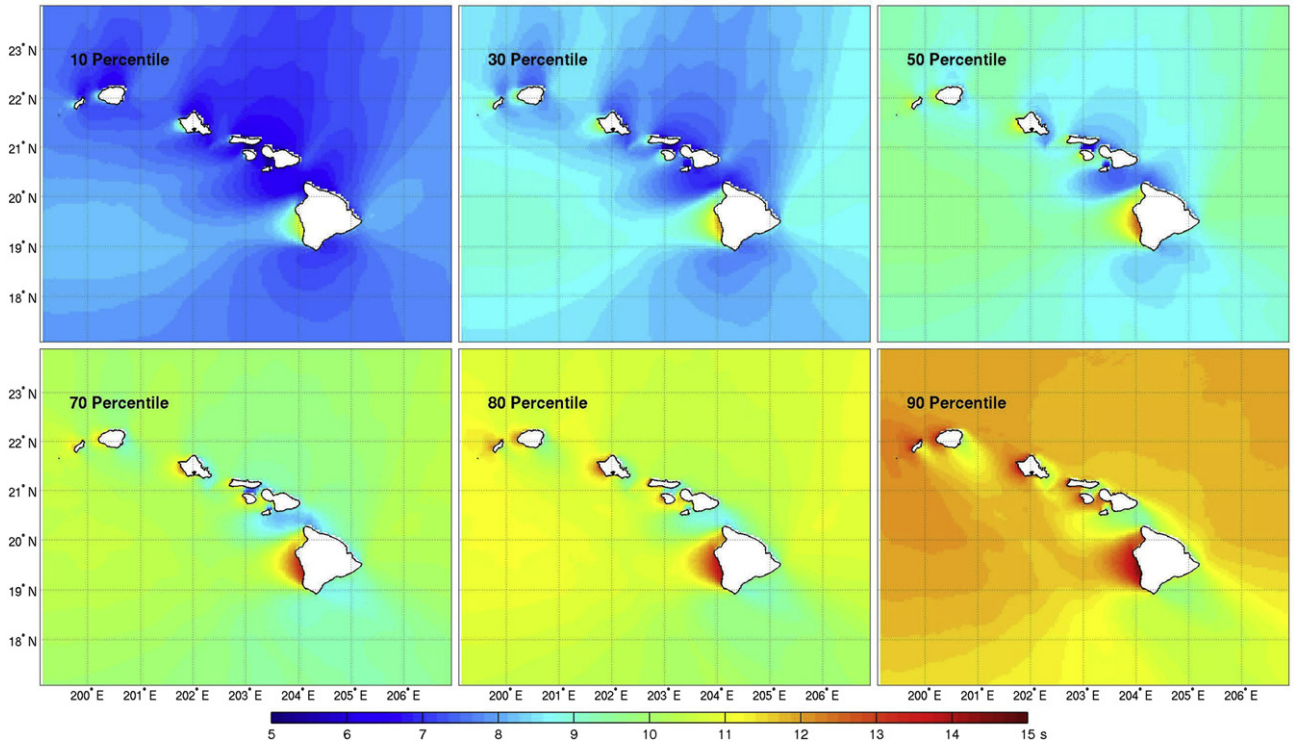

Fig. 11. Percentiles of average wave periods from Hawaii WW3.

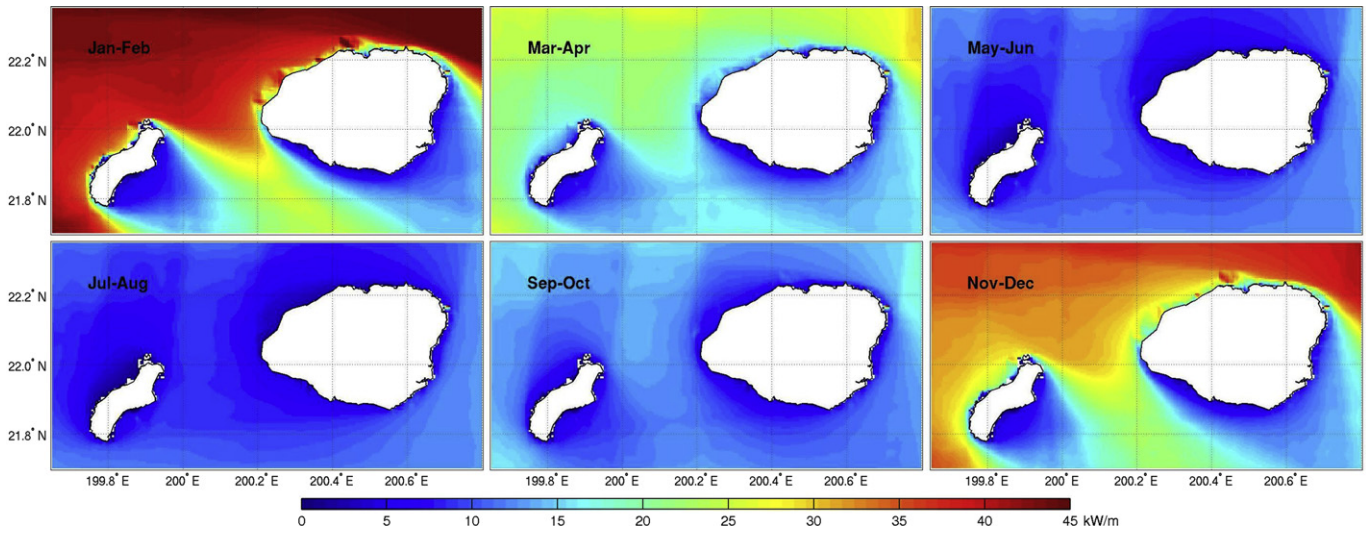

Fig. 12. Bi-monthly median wave power for Kauai.

Hawaii, while buoy 51003 is located in the open ocean to the south. The swells show a general decline in height from north to south across the island chain. Buoy 51201 at 198 m water depth off the north shore of Oahu is partially sheltered from the northwest swell by Kauai and recorded slightly lower or similar wave height comparing to buoy 51003 to the south. Buoy 51202 at 100 m water depth east of Oahu is slightly sheltered from the northwest swells, but fully exposed to the northeast wind waves. The model reproduces the height and timing of the swells and wind waves as well as the slight attenuation of the swell energy from north to south, but underestimates the short duration peak of extreme swells, probably due to the temporal resolution of the FNL data at 6-h intervals. This, however, should have negligible effects on the wave statistics.

Due to the large volume of data, scatter and quantile–quantile (Q–Q) plots are used along with bulk statistics to describe the errors at each buoy. Fig. 7 shows the scatter and Q–Q plots of the data at the four representative buoys for the entire period of 10 years. The linear regression fit in the scatter plots has a slope of less than one, and is consistent with published results in the Pacific [6]. The two blue lines delineate 90% of the data, which is typically within ±0.6 m of the linear regression. The contours, which denote the data density, confirm a general decrease of the wave height across the island chain from north to south. The Q–Q plot, which sorts the recorded and computed wave heights, shows the two datasets follow very similar statistical distributions up to 4–5 m significant wave height. The model tends to underestimate the larger swells at buoys 51001, 51201, and 51202. This might be associated with the low temporal resolution of the input FNL winds that results in omission of short episodic events as illustrated in Fig. 6. The slight overestimation at 51003 is likely due to errors caused by the obstruction coefficients [28], which empirically account for the wave energy reduction through the northwest Hawaiian Islands in Global WW3.

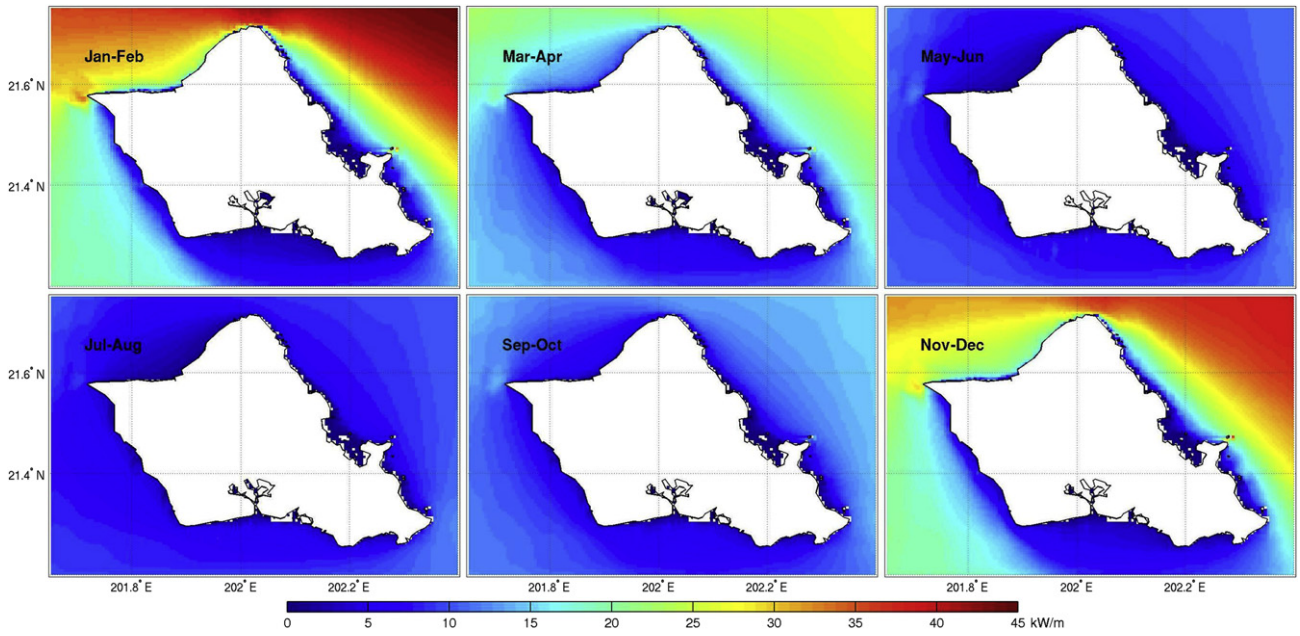

Fig. 13. Bi-monthly median wave power for Oahu.

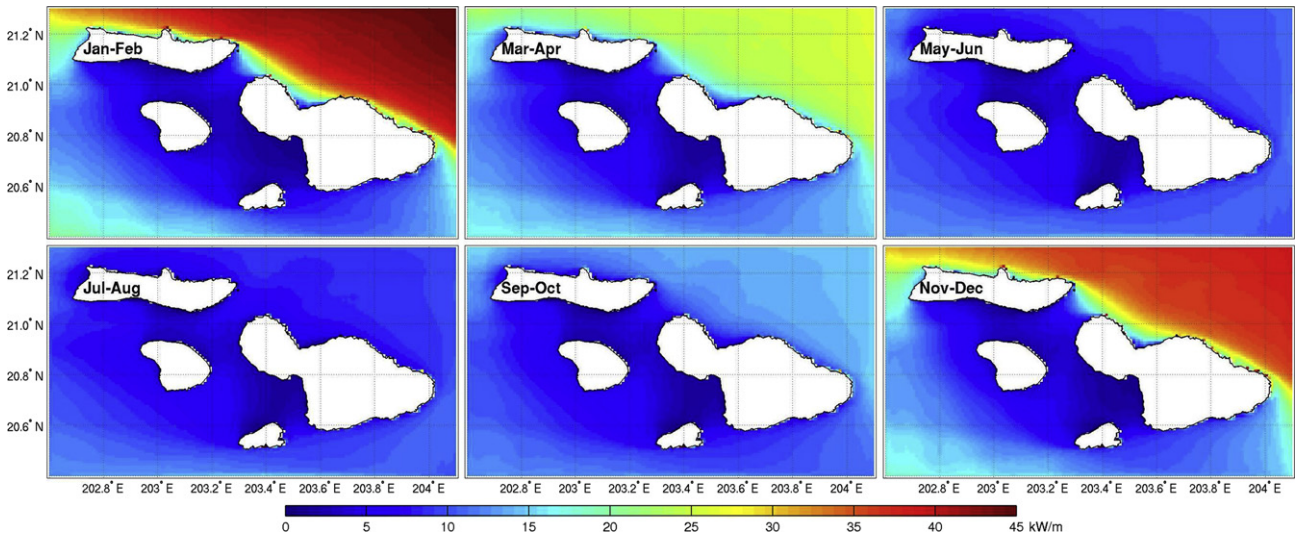

Fig. 14. Bi-monthly median wave power for Maui.

Table 2 provides the error metrics at the 12 buoys to give an overview of the data quality. The model errors indicate the spread of 90% of the data from the linear regression to complement the metrics defined earlier. There is a clear and structured pattern associated with the buoy locations in relation to the dominant wave regimes. The computed significant wave height at buoys 51000, 51001, 51100, and 51101, which are exposed to the northwest swells and northeast wind waves, show uniform and good correlation coefficients of 0.88–0.9 consistent with Tolman et al. [6]. Hawaii WW3 and Oahu SWAN maintain the same level of correlation off the north- and east-facing shores of the islands as inferred from the results at buoys 51201 and 51202. The data quality deteriorates on the lee side of Oahu with a correlation coefficient of 0.84 at buoy 51200. The largest discrepancies occur at KNOH1 on the south shore of Oahu and buoy 51203 on the west side of Lanai. The small slope of the linear fit indicates the model underestimates the wave heights. These discrepancies are most likely due to inadequate energy transfer in the shadow regions due to the approximation of diffraction in the model. The low correlation coefficient of 0.59 at KNOH1 indicates the model does not fully account for the near-shore reef processes in the shallow water depth of 12 m; furthermore the spatial resolution of 560 m is not sufficient to describe wave transformation over the irregular and steep bathymetry. Buoys 51002 and 51003, which are far south of the islands, have

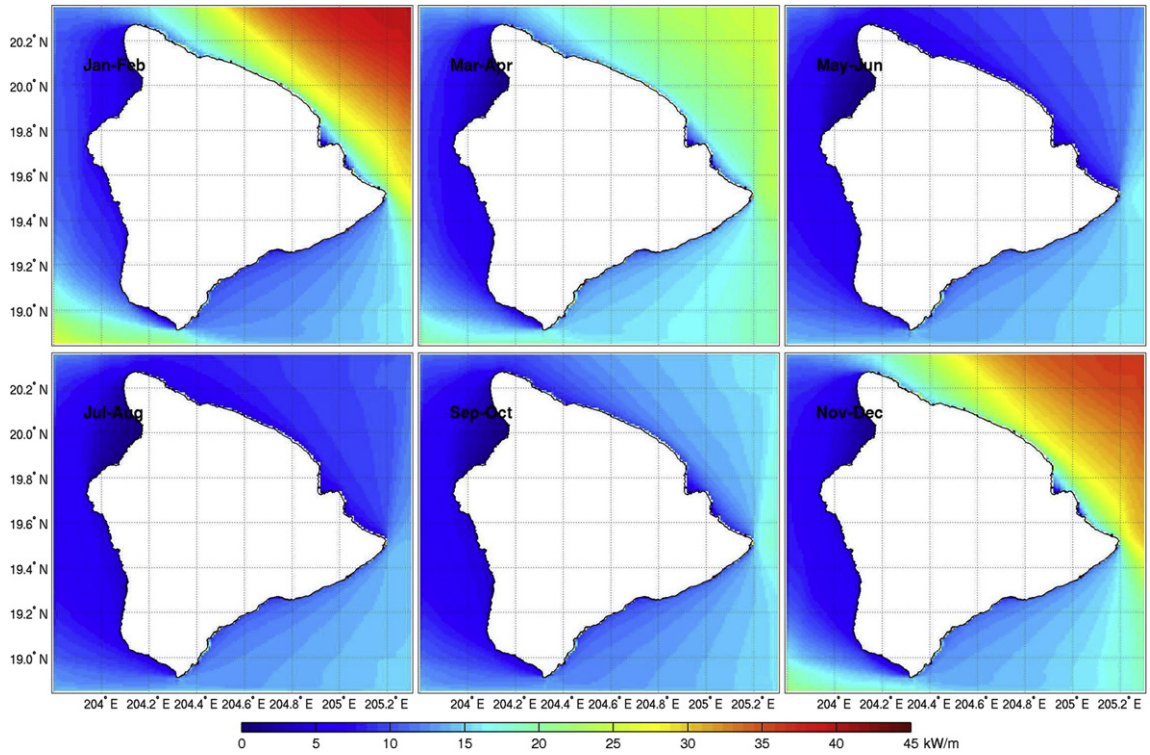

Fig. 15. Bi-monthly median wave power for Hawaii Island.

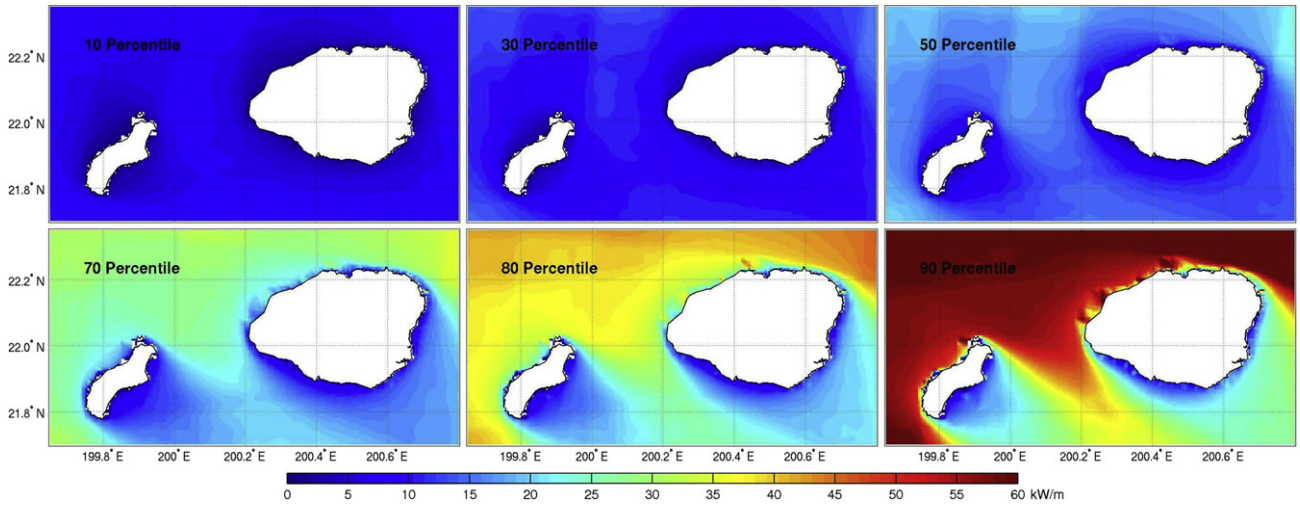

Fig. 16. Percentiles of wave power for Kauai.

similar correlation coefficients of 0.80 and 0.81 respectively. The lower correlation in comparison to their northern counterparts is likely due to the use of the obstruction coefficients to account for the northwest Hawaiian Islands in Global WW3. The higher correlation coefficient of 0.87 at buoy 51004 east of Hawaii Island appears to support this hypothesis.

4.2. Wave climate

The wave climate in Hawaii is defined by the north and south swells superposed on the year-round northeast wind seas. Fig. 8 plots the bi-monthly median significant wave heights from the 10 years of hindcast data to illustrate the seasonal patterns. The northwest swells dominate the winter months from November to February with typical significant wave heights of 3 m. The island chain creates a pronounced shadow of the swell energy. The transition months of March–April reveal similar wave patterns with smaller median wave heights of 2.5 m. During the summer months from May to August, Hawaii experiences gentle south swells. The year-round wind waves of 1–2 m from the northeast produce well-defined shadows on the leeward coasts. Local acceleration of the trade winds increases the wave height in the channels and to the south of Hawaii Island. Local maxima of the wave height develop downstream of the 'Alenuihaha channel and southwest of Hawaii Island in response to the heightened wind speeds in July and August. Subtle effects from the south swells are seen in the waters just north of the Ka'ie'ie Waho channel, between Kauai and Oahu, the Ka'iwi channel, between Oahu and Molokai, and to the east of Hawaii Island, where the larger wave heights are created by combining with the wind waves. September–October sees an overall increase in wave height due to a more direct approach of the south swells as the source shifts westward toward New Zealand [4]. In addition, the Northern Hemisphere has increased swell activities, although small in relation to the January–February episodes. There

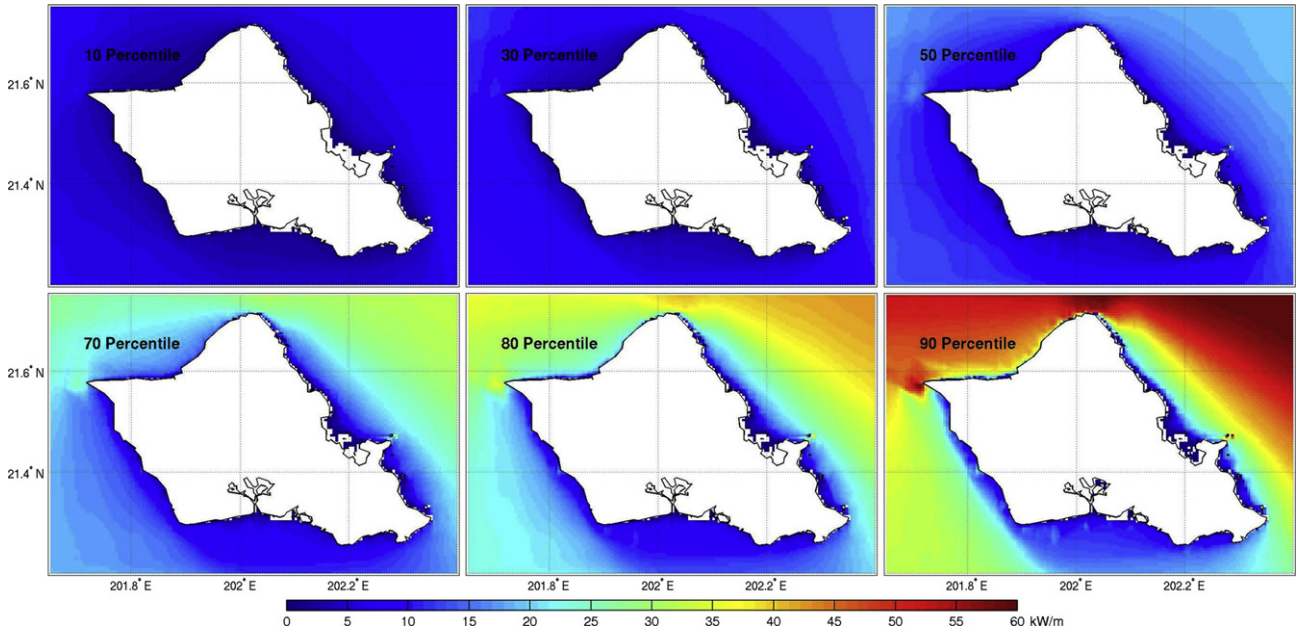

Fig. 17. Percentiles of wave power for Oahu.

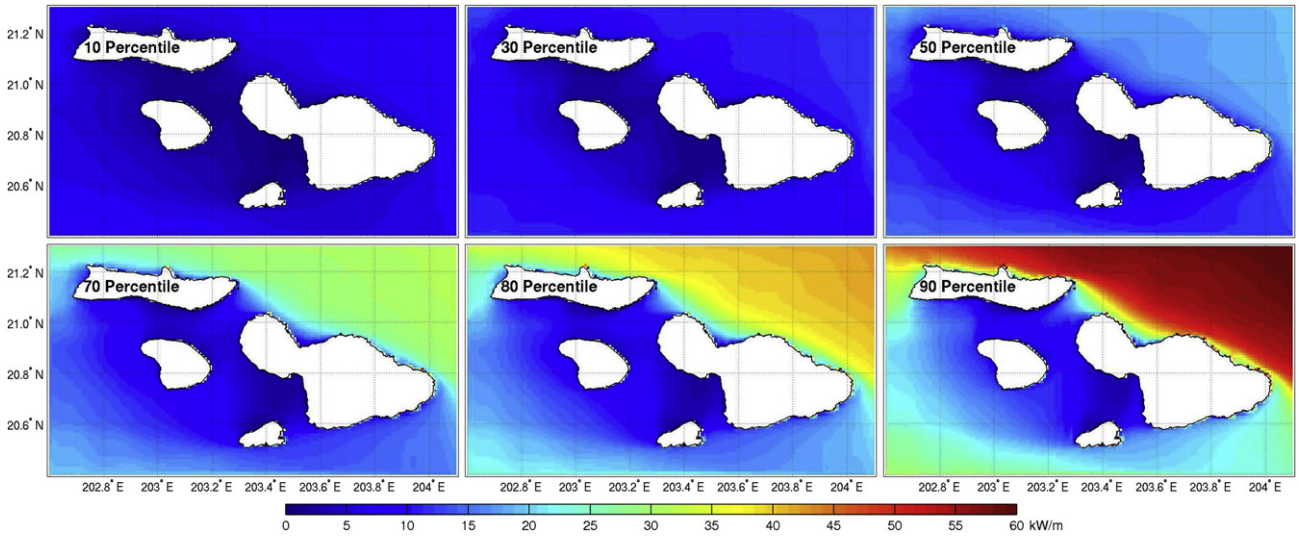

Fig. 18. Percentiles of wave power for Maui.

are no dominant patterns in these months but a combination of all three major components.

The wave period plays an equally important role in defining the available energy resources. While the peak period is commonly used to characterize sea states with a dominant component, we consider the average period, which is more representative of the multi-modal wave climate in Hawaii. Fig. 9 plots the bi-monthly median wave period to provide a different perspective on the wave climate. The northwest swells dominate the pattern in the winter months from November to February with average wave periods over 10 s in exposed waters. The waves generated by the trade winds have shorter periods of 7–8 s as evident in waters off the south-facing shores sheltered from the northwest swell. Local acceleration of the trade winds southwest of Hawaii Island results

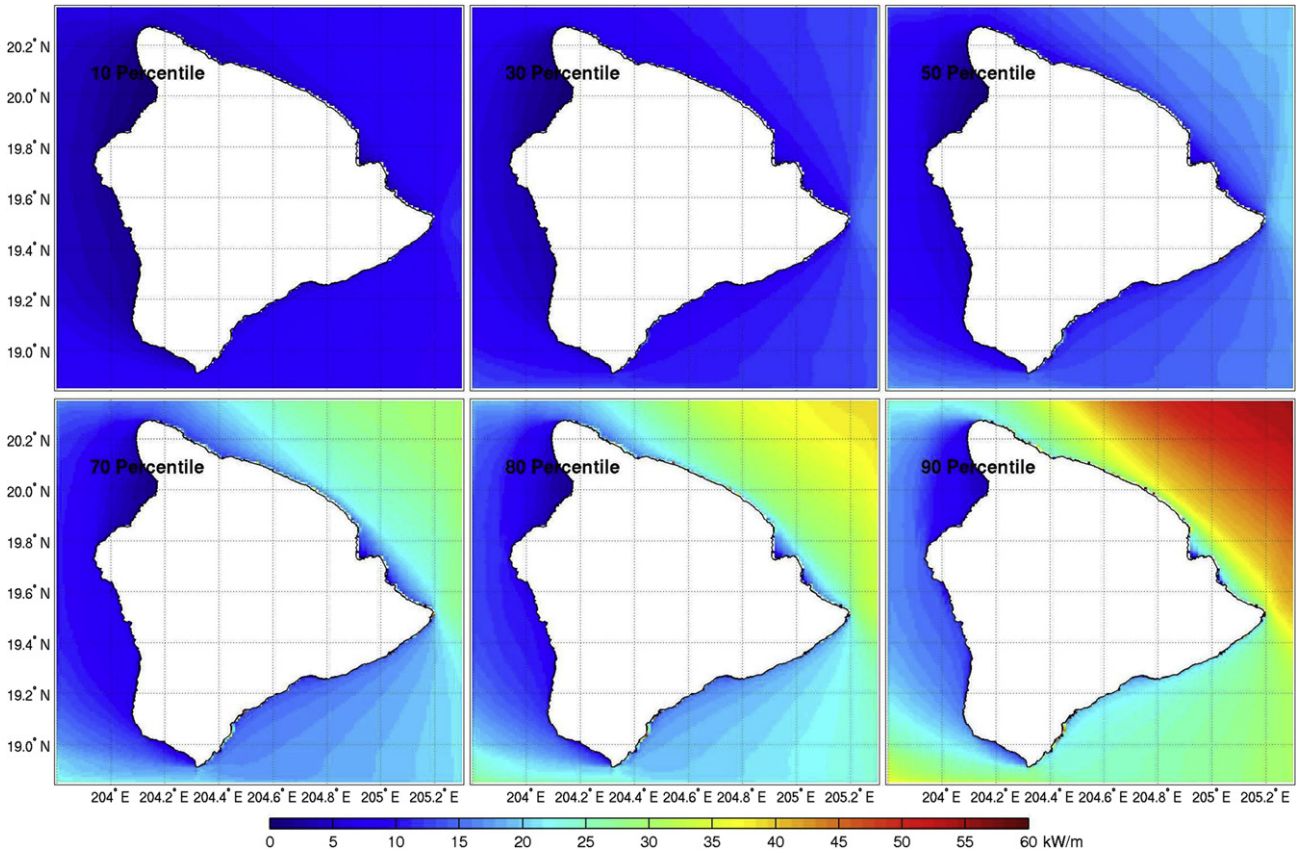

Fig. 19. Percentiles of wave power for Hawaii Island.

in heightened wind wave activities and reduction of the average period over a large region. The west-facing shores, which are sheltered from the trade wind waves, see larger periods associated with the northwest swells. The increase off the west side of Hawaii Island, which is also in the shadow of the northwest swells, is due to the year-round swells generated in the South Pacific. These local increases of the average period persist through the transition months of March and April. In the absence of the northwest swells, the effects of the south swell become more visible with typical wave periods of 6–9 s from May through August. The lower end of the range corresponds to the wind wave period in the shadows of the south swells and the upper end represents the average between the south swells and the wind waves. September–October represents similar features of all seasons and no one wave regime dominates.

Figs. 10 and 11 show the percentile plots to illustrate the overall statistics of the significant wave height and average wave period. The 50-percentile, which has a similar pattern as May–June, represents a transition from wind–wave to north swell dominated conditions. The most prominent feature is a relatively calm region extending from Kauai to Hawaii Island due to sheltering from both the trade wind waves and northwest swells. The northwest swells dominate the top 30% with significant wave heights and average periods larger than 2.5 m and 10 s respectively. The same pattern exists in the bi-monthly plots, where the period is enhanced in the swell dominated regions of the northwest shores of Niihau, Kauai, and Oahu. The waves in the 'Alenuihaha channel, which are dominated by local acceleration of the trade winds, have an average period of 6–8 s 70% of the time. The wave period and significant wave height reach 10 s and 3 m at the 90-percentile confirming the severity of the wind waves in this region. The wave period patterns reveal the presence of south swells produced in the "Roaring Forties" throughout the year [3,4]. Over 90% of the time, the waters slightly west of Hawaii Island experience waves of less than 1.5 m height, but over 11 s period due to swells from the south. The windward shores have wave heights and periods over 2 m and 7 s in comparison. The plots of significant wave height do not show drastic effects of the south swells, which are being overshadowed by the more energetic northwest swells or northeast wind waves.

5. Wave energy resources

The climate analysis has illustrated the seasonal and regional patterns of the wind waves and swells and provided a general assessment of the potential for wave energy development in Hawaii. Site selection is a more delicate design and planning issue because of infrastructure investments and regulatory requirements. Most pre-commercial WEC devices, such as Pelamis and Power Buoy, are designed for nearshore waters around 50–70 m depth to minimize transmission losses and allow for routine maintenance. For implementation in Hawaii, it is currently expected that these devices will require 5 kW/m of wave power to be operational and an annual median of 12 kW/m to be viable. High-resolution estimates of wave power in coastal waters are necessary to identify optimal sites that satisfy these requirements for deployment of WEC devices.

Eq. (2) provides the wave power in coastal waters around the major Hawaiian Islands using SWAN output. Figs. 12–15 show the bi-monthly median wave power in the Kauai, Oahu, Maui, and, Hawaii Island domains from the 10 years of hindcast data. Between November and February, the exposed north shores of all islands receive at least 30 kW/m of wave power from the northwest swells. Most of these shorelines have values above 25 kW/m between the 50- and 70-m depth contours. Wave refraction over the undulating volcanic island slopes modulates the wave energy distribution

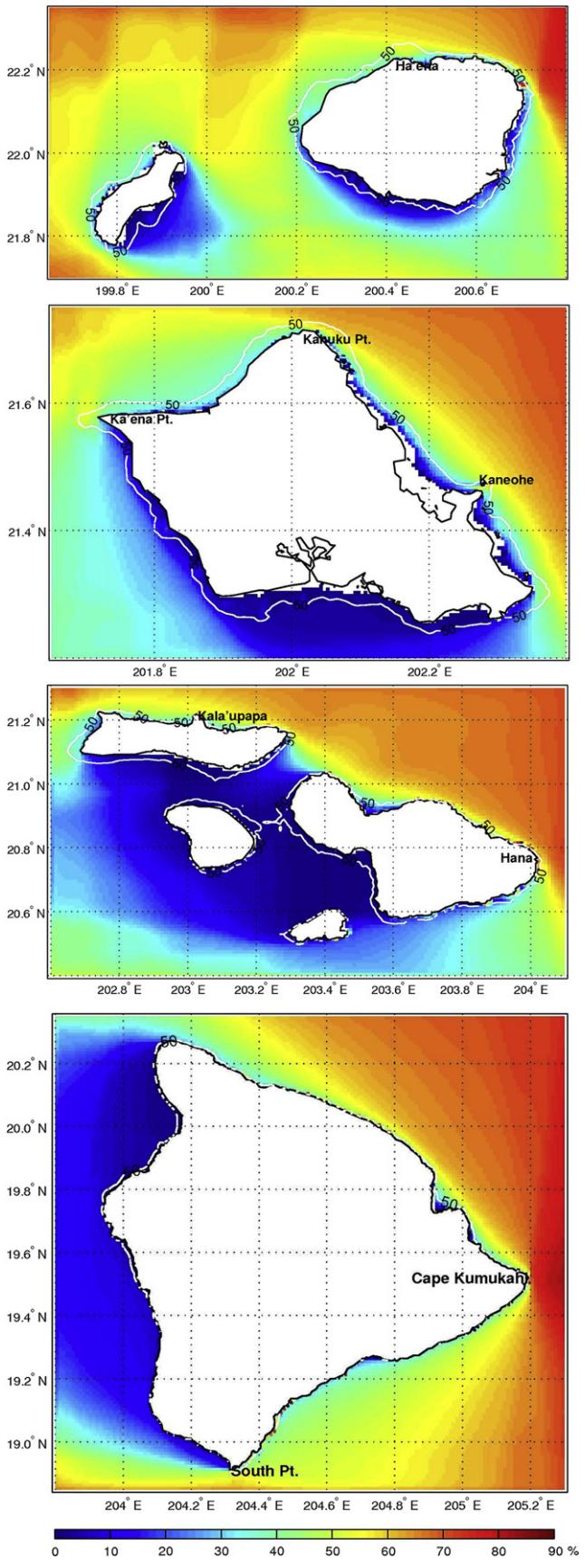

Fig. 20. Frequency of occurrence for $P \geq 12$ kW/m. White line indicates the 50-m depth contour.

along the shore. The wave energy resource for the remainder of the year is moderate despite the year-round northeast wind waves and south swells. The northeast wind waves produce consistent power of 10–15 kW/m between the 50- and 70-m contours of the windward shores from May to October. The south swells are only discernible in the channels between Niihau, Kauai, and Oahu, but not at other locations because they typically have lower energy levels than the wind waves. Stopa et al. [19] showed through partitioning of energy spectra that a large south swell only has 15 kW/m of wave power.

Figs. 16–19 show the percentile plots to illustrate the wave power statistics for planning and operation. The 10-percentile plots, which show relatively uniform power of 5 kW/m over all shorelines, are representative of the gentle south swells and moderate trade wind waves in the summer months. The persistent power above the threshold assures year-round operation of most devices in Hawaii. The 30 and 50 percentiles see increasing contributions of the trade wind waves to the power on the east-facing shores. The north- and east-facing shores generally have annual median power of 15 kW/m or higher between the 50- and 70-m depth contours. The contrast is striking with the 70, 80, and 90 percentiles, which show dramatic north–south asymmetry of the wave energy distribution. The signature of the northwest swells dominates these upper percentiles with 30 kW/m or higher on north-facing shores, except for Hawaii Island, which is partially sheltered by Maui. The 90-percentile plots show 60 kW/m of wave power at selected locations on Kauai and Oahu's north shores, where the underlying bathymetry focuses the wave energy toward the shore.

All renewable energy technologies face difficulties in producing base load power to customers. Although the episodic northwest swells produce high wave power, a consistent energy supply is the key to a successful operation. For illustration, Fig. 20 shows the percentage time when the wave power is over 12 kW/m for economic viability. The southern and western shores on all islands are typically not suitable for WEC devices. It is primarily the year-round wind waves that supply the most consistent energy within the 50- and 70-m depth contours on north- and east-facing shores. The most favorable location on Hawaii Island is Cape Kumukahi, which has 12 kW/m of wave power 82% of the time. Because of the steep volcanic island slope, the 50-m contour is within 100 m from the shore at this location. The east Maui coast near Hana, the north Molokai coast at Kalaupapa, and the north Kauai coast at Heana all have 12 kW/m of wave power for at least 60% of the time. These locations have isolated communities that depend on remote extensions of the power grids, thereby making small-scale renewable energy projects an attractive option.

Oahu has 75% of the state's population and consumes the majority of electricity produced in Hawaii. The island is home to population centers, business districts, tourist destinations, and military installations. Being close to the consumers is a major incentive to any energy resource project. The insular shelf off Kaneohe on the windward shore of Oahu appears to be a favorable site for wave energy development. The coastline is adjacent to a military base on a headland off the vantage point from nearby communities. A region of the insular shelf between the 50- and 70-m contours has 12 kW/m of wave power close to 58% of the time. The site is sheltered from the most severe northwest swells that might damage the devices and their mooring systems, while being open to the more gentle, late-season winter swells from the north. The location has been selected as the Wave Energy Test Site of the Hawaii National Marine Renewable Energy Center with test platforms, mooring systems, power cables, and monitoring buoys extending to about 80 m water depth. The insular shelf off Keana Point and Kahuku Point at the northwest and northeast corner of Oahu has 12 kW/m of wave power 55% of the time, but the locations are open to the severe northwest swells that reach 5 m significant wave height every year.

6. Conclusions

A hindcast study using a system of nested computational models has produced 10 years of regional wind and wave data for climate research and resources assessment in Hawaii. The computed wind data reproduces the omnipresence of the trade winds in Hawaii and the local wind patterns that include decelerating airflows on the windward slopes, accelerating airflow in channels and around headlands, and prominent wake formation leeward of the islands. Comparison with satellite measured wind fields shows good overall agreement of the approaching flow as well as its local deceleration and acceleration around the islands. Discrepancies primarily occurs in the wake region leeward of Hawaii Island due to difficulties in reproducing the timing of the stochastic flows, but those should have secondary effects on the modeled waves and become negligible in the computation of the statistics.

The trade winds produce year-round waves from the east to northeast superposed by episodic swells from the north and south. The wave climate in the winter months is dominated by the northwest swells with median wave heights and periods of 3 m and 11 s. During the summer months, wind waves of 1–2 m height and 7 s period dominate north of the Hawaiian Islands. The acceleration of the trade winds in the 'Alenuihaha Channel and to the south of Hawaii Island increases the local wave height to 2.5 m. Swells from the south are persistent throughout the year, but are only revealed by the increase of the average wave period in the shadows of the north swells and wind waves. The computed significant wave heights show very good correlation with altimetry and buoy data north and east of the island chain, but tend to underestimate the measurements in shadows of the northwest swell and the east to northeast wind waves due to diffraction approximations in the spectral wave model.

The bi-monthly median and percentile plots quantify the available wave power for each of the major islands in Hawaii. The northwest swells in the winter months typically produce 35 kW/m of wave power reaching as high as 50 kW/m 10% of the time. Consistency is a major concern for wave energy devices. The trade wind waves can provide wave power of 12 kW/m within the 50- to 70-m contours on north- and east-facing shores for economic viability. The northwest swells are sufficient to augment the wave power to an annual median above 20 kW/m. Potential sites on Kauai, Maui, and Hawaii Island are adjacent to remote communities and suitable for small-scale wave energy farms. Kaneohe on the windward shore of Oahu is ideal for wave energy development because of its proximity to population centers and the availability of a shallow shelf off the vantage point from accessible areas.

Acknowledgements

The Office of Naval Research funded the development of the wave model package through Grant No. N00014-02-1-0903 and the NOAA Integrated Ocean Observing System Program is supporting its operation through a cooperative agreement NA07NOS4730207 with the University of Hawaii. The Department of Energy funded the wave climate and energy resource study through Grant No. DEFG36-08GO18180 via the Hawaii National Marine Renewable Energy Center. SOEST Contribution Number 8778.

References

[1] Falcao A. Wave energy utilization: a review of technologies. Renewable and Sustainable Energy Reviews 2010;14(3):899–918.

[2] Clément AH, McCullen P, Falcão A, Fiorentino A, Gardner F, Hammarlund K, et al. Wave energy in Europe: current status and perspectives. Renewable and Sustainable Energy Reviews 2002;6(5):405–31.
[3] Arinaga RA, Cheung KF. Atlas of global wave energy from 10 years of reanalysis and hindcast data. Renewable Energy 2012;39(1):49–64.
[4] Stopa JE, Cheung KF, Tolman HL, Chawla A. Patterns and cycles in the climate forecast system reanalysis wind and wave data. Ocean Modelling 2012, http://dx.doi.org/10.1016/j.ocemod.2012.10.005.
[5] Yang Y, Chen YL, Fujioka FM. Numerical simulations of the island-induced circulations over the island of Hawaii during HaRP. Monthly Weather Review 2005;133(12):3693–713.
[6] Tolman HL, Balasubramaniyan B, Burroughs LD, Chalikov DV, Chao YY, Chen HS, et al. Development and implementation of wind generated ocean surface wave models at NCEP. Weather and Forecasting 2002;17(2):311–33.
[7] Tolman HL. A mosaic approach to winds wave modeling. Ocean Modelling 2008;25(1):35–47.
[8] Yang F, Pan HL, Krueger SK, Moorthi S, Lord SJ. Evaluation of the NCEP global forecast system at the ARM SGP site. Monthly Weather Review 2006;134(12):3668–90.
[9] Komen GJ, Cavaleri L, Donelan M, Hasselmann K, Hasselmann S, Janssen PAEM. Dynamics and modelling of ocean waves. Cambridge University Press; 1994. 532 pp.
[10] Caires S, Sterl A, Komen G, Swail V. The web-based KNMI/ERA-40 global wave climatology atlas. Bulletin of the World Meteorological Organization 2004;53(2):142–6.
[11] Ponce de Leon S, Guedes Soares C. On the sheltering effect of Islands in ocean wave models. Journal of Geophysical Research – Oceans 2005;104(C09020):1–17.
[12] Rusu L, Pilar P, Guedes Soares C. Evaluation of wave conditions in Madeira Archipelago with spectral models. Ocean Engineering 2008;35(13):1357–71.
[13] Iglesias G, Lopez M, Carballo R, Fraguela JA, Frigaard P. Wave energy potential in Galicia (NW Spain). Renewable Energy 2009;31(2):2323–33.
[14] Waters R, Engstrom J, Isberg J, Leijon M. Wave climate off Swedish west coast. Renewable Energy 2009;34(6):1600–6.
[15] Rusu L, Guedes Soares C. Wave energy assessments in the Azores Islands. Renewable Energy 2012;45:183–96.
[16] Wilson JH, Beyene A. California wave energy resource evaluation. Journal of Coastal Research 2007;233(3):679–90.
[17] Define Z, Haas KA, Fritz HM. Wave power potential along the Atlantic coast of the southeastern USA. Renewable Energy 2009;34(10):2197–205.
[18] Hemer MA, Griffin DA. The wave energy resource along Australia's Southern margin. Journal of Renewable Sustainable Energy 2010, http://dx.doi.org/10.1063/1.3464753.
[19] Stopa JE, Cheung KF, Chen Y-L. Assessment of wave energy resources in Hawaii. Renewable Energy 2011;36(2):554–67.
[20] Skamarock WC. Evaluating mesoscale NWP models using kinetic energy spectra. Monthly Weather Review 2004;132(12):3019–32.
[21] Zhang Y, Chen YL, Kodama K. Validation of the coupled NCEP mesoscale spectral model and an advanced land surface model over the Hawaiian Islands. Part II: a high wind event. Weather and Forecasting 2005;20(6):873–95.
[22] Booij N, Ris RC, Holthuijsen LH. A third-generation wave model for coastal regions, Part I, model description and validation. Journal of Geophysical Research – Oceans 1999;104(C4):7649–66.
[23] Holthuijsen LH, Herman A, Booij N. Phase-coupled refraction-diffraction for spectral wave models. Coastal Engineering 2003;49(4):291–305.
[24] Filipot J-F, Cheung KF. Spectral wave modeling in fringing reef environments. Coastal Engineering 2012;67:67–79.
[25] Chelton DB, Freilich MH. Scatterometer-based assessment of 10-m wind analyses from the operational ECMWF and NCEP numerical weather prediction models. Monthly Weather Review 2005;133(2):409–29.
[26] Zhang Y, Chen YL, Hong SY, Juang MH, Kodama K. Validation of the coupled NCEP mesoscale spectral model and an advanced land surface model over the Hawaiian Islands. Part I: summer trade wind conditions and a heavy rainfall event. Weather and Forecasting 2005;20(6):847–72.
[27] Ardhuin F, Rogers E, Babanin AV, Filipot J-F, Magne R, Roland A, et al. Semi-empirical dissipation source functions for ocean waves part I: definition, calibration, and validation. Journal of Physical Oceanography 2010;40(9):1917–41.
[28] Tolman HL. Treatment of unresolved islands and ice in wind wave models. Ocean Modelling 2003;5(3):219–31.
[29] JPL. QuikSCAT science data product user's manual. Jet Propulsion Laboratory; 2000. Publication D-18053: 84 pp.
[30] Ebuchi N, Graber NC, Caruso MJ. Evaluation of wind vectors observed by QuikSCAT/seawinds using ocean buoy data. Journal of Atmospheric Oceanic Technology 2002;19(12):2049–62.
[31] Fedor LS, Godbey TW, Gower JF, Guptill R, Hayne GS, Rufenach CL, et al. Satellite altimeter measurements of sea state – an algorithm comparison. Journal of Geophysical Research – Solid Earth 1979;84(B8):3991–4001.
[32] Smith RB, Grubišić V. Aerial observation of Hawaii's wake. Journal of Atmospheric Science 1993;50(11):3728–50.
[33] Yang Y, Chen YL. Circulations and rainfall on the leeside of the island of Hawaii during HaRP. Monthly Weather Review 2003;131(10):2525–42.
[34] Carlis DL, Chen YL, Morris V. Numerical simulations of island-scale airflow and the Maui vortex during summer trade-wind conditions. Monthly Weather Review 2010;138(7):2706–36.
[35] Tu CC, Chen YL. Favorable conditions for the development of a heavy rainfall event over Oahu during the 2006 wet period. Weather and Forecasting 2011;26(3):280–300.
[36] Xie SP, Liu WT, Liu Q, Nonaka M. Far-reaching effects of the Hawaiian islands on the Pacific Ocean-atmosphere system. Science 2001;292(5524):2057–60.